

# A compact fission detector for fission-tagging neutron capture experiments with radioactive fissile isotopes

---

(n\_TOF Collaboration) Bacak, M.; Aïche, M.; Bélier, G.; Berthoumieux, E.; Diakaki, M.; Dupont, E.; Günsing, F.; Heyse, J.; Kopecky, S.; Laurent, B.; ...

Source / Izvornik: **Nuclear Instruments and Methods in Physics Research Section A: Accelerators, Spectrometers, Detectors and Associated Equipment, 2020, 969**

Journal article, Published version

Rad u časopisu, Objavljena verzija rada (izdavačev PDF)

<https://doi.org/10.1016/j.nima.2020.163981>

Permanent link / Trajna poveznica: <https://urn.nsk.hr/urn:nbn:hr:217:174944>

Rights / Prava: [Attribution 4.0 International](#)/[Imenovanje 4.0 međunarodna](#)

Download date / Datum preuzimanja: **2024-07-15**



Repository / Repozitorij:

[Repository of the Faculty of Science - University of Zagreb](#)





## A compact fission detector for fission-tagging neutron capture experiments with radioactive fissile isotopes

M. Bacak<sup>1,2,3,\*</sup>, M. Aïche<sup>4</sup>, G. Bélier<sup>5</sup>, E. Berthoumieux<sup>3</sup>, M. Diakaki<sup>3</sup>, E. Dupont<sup>3</sup>, F. Gunsing<sup>3,1</sup>, J. Heyse<sup>6</sup>, S. Kopecky<sup>6</sup>, B. Laurent<sup>5</sup>, H. Leeb<sup>2</sup>, L. Mathieu<sup>4</sup>, A. Moens<sup>6</sup>, S. Richter<sup>6</sup>, P. Schillebeeckx<sup>6</sup>, O. Serot<sup>7</sup>, G. Sibbens<sup>6</sup>, J. Taieb<sup>5</sup>, D. Vanleeuw<sup>6</sup>, V. Vlachoudis<sup>1</sup>, O. Aberle<sup>1</sup>, S. Amaducci<sup>8,9</sup>, J. Andrzejewski<sup>10</sup>, L. Audouin<sup>11</sup>, J. Balibrea<sup>12</sup>, M. Barbagallo<sup>13</sup>, F. Bečvář<sup>14</sup>, J. Billowes<sup>15</sup>, D. Bosnar<sup>16</sup>, A. Brown<sup>17</sup>, M. Caamaño<sup>18</sup>, F. Calviño<sup>19</sup>, M. Calviani<sup>1</sup>, D. Cano-Ott<sup>12</sup>, R. Cardella<sup>1</sup>, A. Casanovas<sup>19</sup>, F. Cerutti<sup>1</sup>, Y.H. Chen<sup>11</sup>, E. Chiaveri<sup>1,15,20</sup>, N. Colonna<sup>13</sup>, G. Cortés<sup>19</sup>, M.A. Cortés-Giraldo<sup>20</sup>, L. Cosentino<sup>21</sup>, L.A. Damone<sup>13,22</sup>, C. Domingo-Pardo<sup>23</sup>, R. Dressler<sup>24</sup>, I. Durán<sup>18</sup>, B. Fernández-Domínguez<sup>18</sup>, A. Ferrari<sup>1</sup>, P. Ferreira<sup>25</sup>, P. Finocchiaro<sup>21</sup>, V. Furman<sup>26</sup>, K. Göbel<sup>27</sup>, A.R. García<sup>12</sup>, A. Gawlik<sup>10</sup>, S. Gilardoni<sup>1</sup>, T. Glodariu<sup>28,a</sup>, I.F. Gonçalves<sup>25</sup>, E. González-Romero<sup>12</sup>, E. Griesmayer<sup>2</sup>, C. Guerrero<sup>20</sup>, H. Harada<sup>29</sup>, S. Heinitz<sup>24</sup>, D.G. Jenkins<sup>17</sup>, E. Jericha<sup>2</sup>, F. Käppeler<sup>30</sup>, Y. Kadi<sup>1</sup>, A. Kalamara<sup>31</sup>, P. Kavragin<sup>2</sup>, A. Kimura<sup>29</sup>, N. Kivel<sup>24</sup>, I. Knapova<sup>14</sup>, M. Kokkoris<sup>31</sup>, M. Krtička<sup>14</sup>, D. Kurtulgil<sup>27</sup>, E. Leal-Cidoncha<sup>18</sup>, C. Lederer<sup>32</sup>, J. Lerendegui-Marco<sup>20</sup>, S. Lo Meo<sup>33,8</sup>, S.J. Lonsdale<sup>32</sup>, D. Macina<sup>1</sup>, A. Manna<sup>8,9</sup>, J. Marganec<sup>10,34</sup>, T. Martínez<sup>12</sup>, A. Masi<sup>1</sup>, C. Massimi<sup>8,9</sup>, P. Mastinu<sup>35</sup>, M. Mastromarco<sup>13</sup>, E.A. Maugeri<sup>24</sup>, A. Mazzone<sup>13,36</sup>, E. Mendoza<sup>12</sup>, A. Mengoni<sup>33</sup>, P.M. Milazzo<sup>37</sup>, F. Mingrone<sup>1</sup>, A. Musumarra<sup>21,38</sup>, A. Negret<sup>28</sup>, R. Nolte<sup>34</sup>, A. Oprea<sup>28</sup>, N. Patronis<sup>39</sup>, A. Pavlik<sup>40</sup>, J. Perkowski<sup>10</sup>, I. Porras<sup>41</sup>, J. Praena<sup>41</sup>, J.M. Quesada<sup>20</sup>, D. Radeck<sup>34</sup>, T. Rauscher<sup>42,43</sup>, R. Reifarth<sup>27</sup>, C. Rubbia<sup>1</sup>, J.A. Ryan<sup>15</sup>, M. Sabaté-Gilarte<sup>1,20</sup>, A. Saxena<sup>44</sup>, D. Schumann<sup>24</sup>, P. Sedyshev<sup>26</sup>, A.G. Smith<sup>15</sup>, N.V. Sosnin<sup>15</sup>, A. Stamatopoulos<sup>31</sup>, G. Tagliente<sup>13</sup>, J.L. Tain<sup>23</sup>, A. Tarifeño-Saldivia<sup>19</sup>, L. Tassan-Got<sup>11</sup>, S. Valenta<sup>14</sup>, G. Vannini<sup>8,9</sup>, V. Variale<sup>13</sup>, P. Vaz<sup>25</sup>, A. Ventura<sup>8</sup>, R. Vlastou<sup>31</sup>, A. Wallner<sup>45</sup>, S. Warren<sup>15</sup>, C. Weiss<sup>2</sup>, P.J. Woods<sup>32</sup>, T. Wright<sup>15</sup>, P. Žugec<sup>16,1</sup>

<sup>1</sup> European Organization for Nuclear Research (CERN), Switzerland

<sup>2</sup> Technische Universität Wien, Austria

<sup>3</sup> CEA Irfu, Université Paris-Saclay, F-91191 Gif-sur-Yvette, France

<sup>4</sup> CENBG, CNRS/IN2P3-Université de Bordeaux, Gradignan, France

<sup>5</sup> CEA, DAM, DIF, F-91297 Arpajon, France

<sup>6</sup> European Commission, Joint Research Centre, Geel, Retieseweg 111, B-2440 Geel, Belgium

<sup>7</sup> CEA, DEN, Cadarache, France

<sup>8</sup> Istituto Nazionale di Fisica Nucleare, Sezione di Bologna, Italy

<sup>9</sup> Dipartimento di Fisica e Astronomia, Università di Bologna, Italy

<sup>10</sup> University of Lodz, Poland

<sup>11</sup> Institut de Physique Nucléaire, CNRS-IN2P3, Univ. Paris-Sud, Université Paris-Saclay, F-91406 Orsay Cedex, France

<sup>12</sup> Centro de Investigaciones Energéticas Medioambientales y Tecnológicas (CIEMAT), Spain

<sup>13</sup> Istituto Nazionale di Fisica Nucleare, Sezione di Bari, Italy

<sup>14</sup> Charles University, Prague, Czech Republic

<sup>15</sup> University of Manchester, United Kingdom

<sup>16</sup> Department of Physics, Faculty of Science, University of Zagreb, Zagreb, Croatia

<sup>17</sup> University of York, United Kingdom

<sup>18</sup> University of Santiago de Compostela, Spain

\* Corresponding author at: European Organization for Nuclear Research (CERN), Switzerland.

E-mail address: [michael.bacak@cern.ch](mailto:michael.bacak@cern.ch) (M. Bacak).

<sup>a</sup> Deceased.

<https://doi.org/10.1016/j.nima.2020.163981>

Received 27 February 2020; Received in revised form 15 April 2020; Accepted 16 April 2020

Available online 21 April 2020

0168-9002/© 2020 The Authors. Published by Elsevier B.V. This is an open access article under the CC BY license

(<http://creativecommons.org/licenses/by/4.0/>).

<sup>19</sup> Universitat Politècnica de Catalunya, Spain<sup>20</sup> Universidad de Sevilla, Spain<sup>21</sup> INFN Laboratori Nazionali del Sud, Catania, Italy<sup>22</sup> Dipartimento di Fisica, Università degli Studi di Bari, Italy<sup>23</sup> Instituto de Física Corpuscular, CSIC - Universidad de Valencia, Spain<sup>24</sup> Paul Scherrer Institut (PSI), Villigen, Switzerland<sup>25</sup> Instituto Superior Técnico, Lisbon, Portugal<sup>26</sup> Joint Institute for Nuclear Research (JINR), Dubna, Russia<sup>27</sup> Goethe University Frankfurt, Germany<sup>28</sup> Horia Hulubei National Institute of Physics and Nuclear Engineering, Romania<sup>29</sup> Japan Atomic Energy Agency (JAEA), Tokai-mura, Japan<sup>30</sup> Karlsruhe Institute of Technology, Campus North, IKP, 76021 Karlsruhe, Germany<sup>31</sup> National Technical University of Athens, Greece<sup>32</sup> School of Physics and Astronomy, University of Edinburgh, United Kingdom<sup>33</sup> Agenzia nazionale per le nuove tecnologie (ENEA), Bologna, Italy<sup>34</sup> Physikalisch-Technische Bundesanstalt (PTB), Bundesallee 100, 38116 Braunschweig, Germany<sup>35</sup> Istituto Nazionale di Fisica Nucleare, Sezione di Legnaro, Italy<sup>36</sup> Consiglio Nazionale delle Ricerche, Bari, Italy<sup>37</sup> Istituto Nazionale di Fisica Nucleare, Sezione di Trieste, Italy<sup>38</sup> Dipartimento di Fisica e Astronomia, Università di Catania, Italy<sup>39</sup> University of Ioannina, Greece<sup>40</sup> University of Vienna, Faculty of Physics, Vienna, Austria<sup>41</sup> University of Granada, Spain<sup>42</sup> Department of Physics, University of Basel, Switzerland<sup>43</sup> Centre for Astrophysics Research, University of Hertfordshire, United Kingdom<sup>44</sup> Bhabha Atomic Research Centre (BARC), India<sup>45</sup> Australian National University, Canberra, Australia

## ARTICLE INFO

## Keywords:

Fission detector

<sup>233</sup>U

n\_TOF

Time-of-flight

## ABSTRACT

In the measurement of neutron capture cross-sections of fissile isotopes, the fission channel is a source of background which can be removed efficiently using the so-called *fission-tagging* or *fission-veto technique*. For this purpose a new compact and fast fission chamber has been developed. The design criteria and technical description of the chamber are given within the context of a measurement of the  $^{233}\text{U}(n, \gamma)$  cross-section at the n\_TOF facility at CERN, where it was coupled to the n\_TOF Total Absorption Calorimeter. For this measurement the fission detector was optimized for time resolution, minimization of material in the neutron beam and for alpha-fission discrimination. The performance of the fission chamber and its application as a fission tagging detector are discussed.

## 1. Introduction

The neutron capture cross-sections of fissile isotopes are of interest in nuclear reactor as they influence the neutron economy of the reactor. However, the knowledge of those cross-sections is limited due to difficulties associated to the background from the fission reaction channel. For the fissile isotopes  $^{233}\text{U}$ ,  $^{235}\text{U}$  and  $^{239}\text{Pu}$  the fission cross-section is on average a factor 2 to 10 larger than their respective capture cross-section, depending on the isotope and energy range, which is shown in Fig. 1. This implies that in a measurement of the capture cross-section the  $\gamma$ -rays coming from the fission channel are a major source of background, which has to be taken care of in the analysis. In the past [1] a method of efficiently dealing with this source of background has been developed, the so-called *fission-tagging* or *fission-veto technique*. In addition to the  $\gamma$ -detector this technique employs a fission detector to measure the fission fragments. The  $\gamma$ -rays from the fission reaction can then be identified or tagged by operating the two detectors in coincidence. In recent years new efforts have been made to measure the capture cross-sections of the fissile isotopes using the *fission-tagging* technique at different facilities [2–5]. Despite *fission-tagging* technique's effectiveness in dealing with the fission background, it has the drawback of introducing another component to the background, namely the sample substrates and the detector itself. In the recent measurements performed at n\_TOF a Micromegas based detector was used as a fission detector [2,4]. The so-called *micro-mesh* of such a detector is made out of copper, which is a significant source of background due to its large scattering and capture cross-sections. With the goal of measuring the  $^{233}\text{U}(n, \gamma)$  cross-section a new fission detector was designed aiming at reducing the background from the detector and

providing the necessary performance to reliably identify the fission  $\gamma$ -rays. The design of the described fission chamber (FICH) is adapted to the measurement of the  $^{233}\text{U}(n, \gamma)$  utilizing the fission chamber coupled to the n\_TOF Total Absorption Calorimeter (TAC) [6] in experimental area 1 (EAR1) of the n\_TOF facility [7].

## 2. The multi-plate fission chamber

Due to the experience obtained from the measurement with the *fission-tagging* micromegas detectors [2,4], a simple ionization cell geometry is chosen as the basic detector design to minimize the material in beam. The development of the fission chamber is focused on different, partially contradictory, criteria: excellent time resolution for the coincidence and time-of-flight measurement; low quantities of structural material to avoid additional background for the capture measurement; reasonable amount of  $^{233}\text{U}$  to obtain a sufficient count rate for high statistics measurements; compact design as the fission chamber (FICH) must fit inside the TAC of n\_TOF. All these requirements are detailed in the following sections.

## 2.1. Technical description

As a result the fission chamber (FICH) is designed as a multi-plate ionization chamber containing two stacks of axial ionization cells. Figs. 2 and 3 show CAD drawings and pictures of the chamber. The housing is made of a 1.5 mm thick aluminium tube with an outer diameter of 66 mm and a length of 78 mm. With a maximum outer diameter of 90 mm and a total length of 120 mm including the flanges with the gas connections and windows, it fits nicely in the  $\gamma$ -calorimeter leaving sufficient space for its absorber (explained in Section 3.1.2) and the connecting beam pipes. Two stacks of seven ionization cells

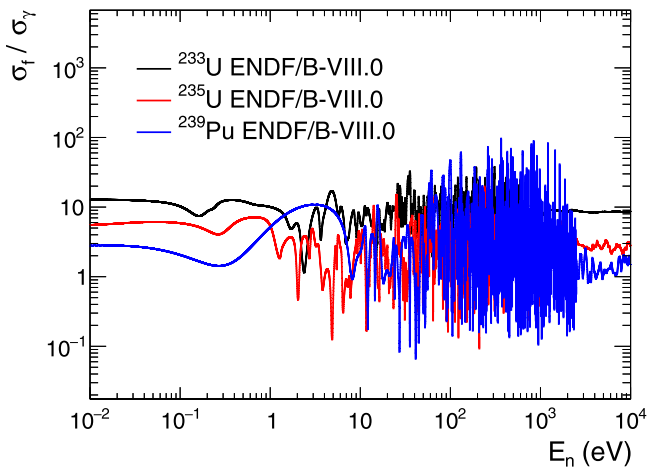


Fig. 1. Cross-section ratios of the fission  $\sigma_f$  and capture  $\sigma_\gamma$  channels for the fissile isotopes  $^{233}\text{U}$ ,  $^{235}\text{U}$  and  $^{239}\text{Pu}$ .

each are mounted directly on their respective motherboards and are inserted from each end of the chamber. The stacks have a minimum inner diameter of 50 mm leaving enough space for the n\_TOF neutron beam with a FWHM of roughly 16 mm and a total width of less than 40 mm. In total 8 anodes are collecting signals from 14  $^{233}\text{U}$  targets deposited on the cathodes. The arrangement of the cathodes, anodes and deposits is illustrated in Fig. 4. To avoid cross-talk from alpha-particles, the ionization cells are separated by 20  $\mu$  aluminium, either one 20  $\mu$  anode foil or two 10  $\mu$  cathode foils, resulting in a total of 300  $\mu$

aluminium in the neutron beam which is a negligible neutron beam perturbation. The chamber is closed with aluminized 25  $\mu$  thick Kapton windows to provide a Faraday cage.

## 2.2. Choice of gas and gas system

The gas is of high importance and has to exhibit a high drift velocity and provide the best possible alpha-fission separation. High purity tetrafluoromethane  $\text{CF}_4$  is a fast gas and is often used where high count rates are expected [8] but has the drawback of being electro-negative, worsening the energy resolution and hence the alpha-fission discrimination. Nevertheless, the advantage it offers due to its higher drift velocity compared to other gases outweighs the disadvantages. Fission fragments (FF) and  $\alpha$ -particles deposit their energy in the gap between the electrodes filled with the gas. Simulations [8] have shown that a gap distance of about 1.5 mm is sufficient to achieve a reasonable alpha-fission separation for  $^{252}\text{Cf}$ . Due to mechanical considerations the gap is chosen to be 3 mm. To achieve a drift velocity of about 11 cm/ $\mu$ s an electric field of 1400 V/cm is applied at atmospheric pressure. This drift velocity corresponds to a total electron drift time of 27 ns in the 3 mm gap, leading to a suitable intrinsic time resolution. In order to guarantee stable conditions throughout the measurement period of four weeks a gas pressure and flow regulation system was employed and is schematically shown in Fig. 5. The fission chamber was operated with a constant gas flow of 0.1 l/min and at an absolute pressure of 1100 mbar to allow for the use of thin windows of the fission chamber, hence to reduce the background in the  $\gamma$ -calorimeter.

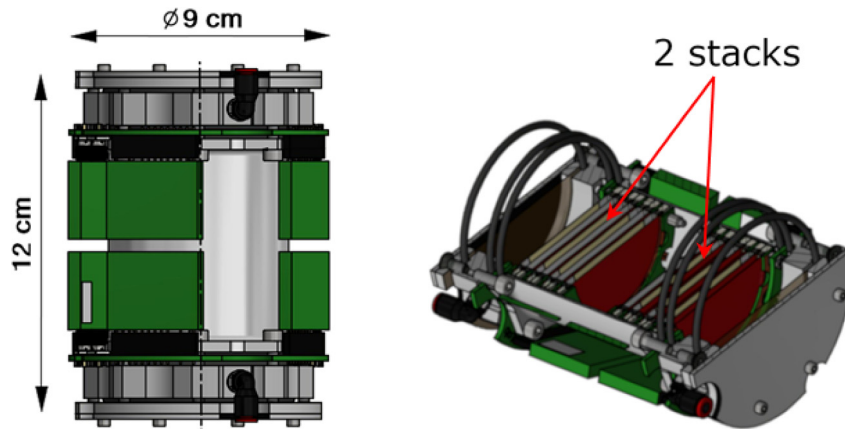


Fig. 2. CAD drawings of the fission chamber and a sectional view. The green blocks around the chamber represent the preamplifiers.

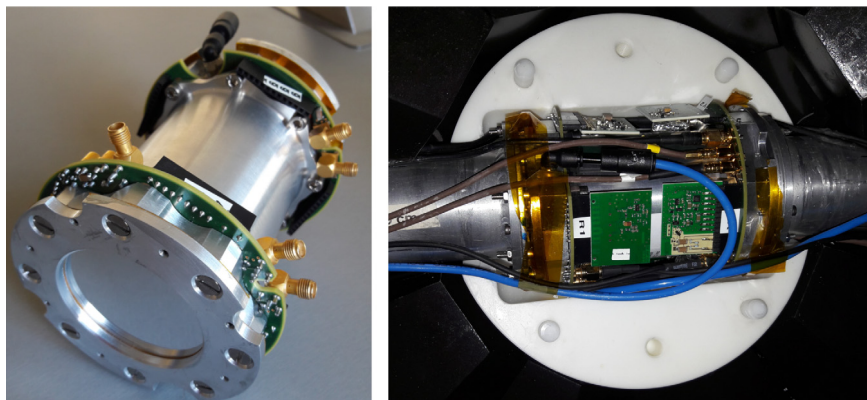


Fig. 3. Pictures of the fission chamber in the lab (left) and embedded in one half of the TAC absorber (white) with electronics and gas supply connected (right).

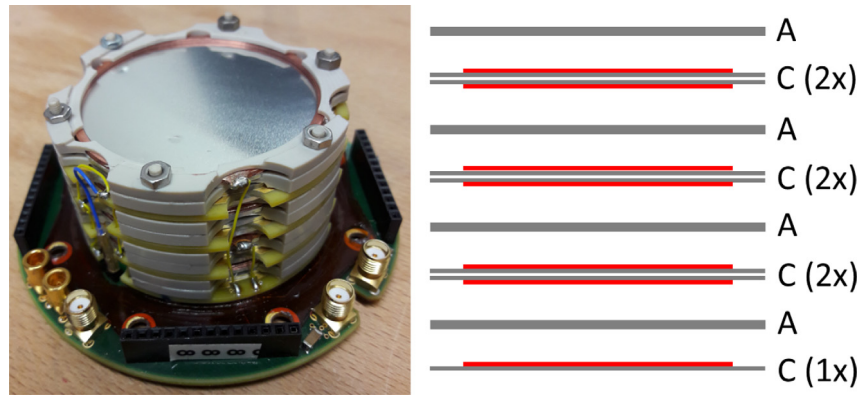


Fig. 4. Picture of one of the two stacks of ionization cells mounted on the motherboard (left). Arrangement of the cathodes (C) and anodes (A) of one stack (right), <sup>233</sup>U deposits are indicated in red. There is one anode that reads only from 1 deposit while the others read signals from two deposits.

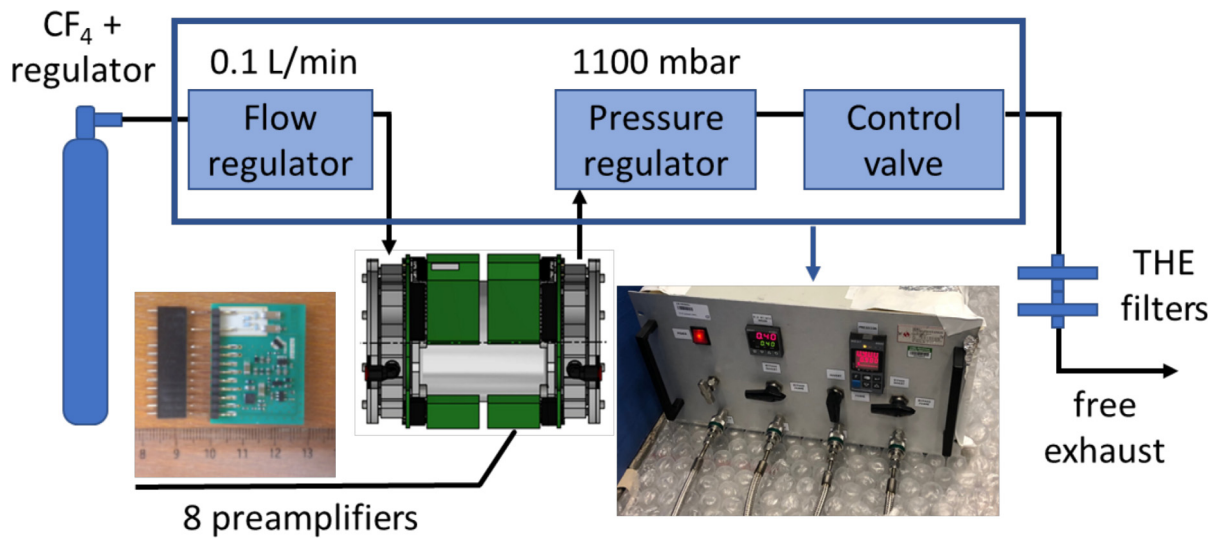


Fig. 5. Schematic illustration of the full FICH set-up including the chamber, a schematic drawing of the gas system, and pictures of one preamplifier-filter printed circuit board (PCB) and of the gas regulation system with the gas filters (THE).

2.3. Dedicated electronics

To ensure a good time resolution and reduce potential  $\alpha$ -particle pile-up, fast electronics adapted to the geometry of the ionization cells and the electron drift velocity have been developed. Charge preamplifiers with a short RC decay time constant have been developed to ensure good amplitude discrimination, avoid saturation due to very high alpha activity and to preserve the good timing response of the chamber. A dedicated card combining the preamplifier and a fast timing filter amplifier was directly mounted on the fission chamber. This reduces the input capacitance and improves the signal-to-noise ratio. A picture of those cards can be seen in the lower left part of Fig. 5. The signals recorded by the data acquisition system were digitized, stored and processed offline using the pulse shape analysis routine developed by the n\_TOF collaboration [9]. An example of a typical signal of a fission fragment is shown in Fig. 6 with a full width at half maximum (FWHM) of 34 ns and a rise time (10-90 %) of 16 ns.

2.4. Fissile deposits

Thin uranium oxide layers, with 99.9361 % enrichment in <sup>233</sup>U, had a diameter of  $40.00 \pm 0.02$  mm and were molecular plated on  $10 \mu$  thick aluminium foils at JRC-Geel. The impurities in the sample have a negligible effect on fission. Nevertheless, a small effect on the <sup>233</sup>U  $\alpha$ -ratio is expected due to the first capture resonance of <sup>234</sup>U at 5.15 eV.

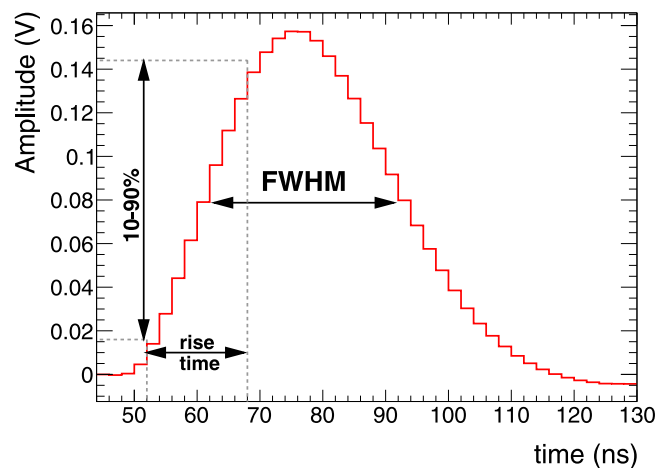


Fig. 6. Average shape of a fission fragment signal from the FICH.

This contribution can be taken into account during the resonance analysis. The activity of each of the 14 samples hosted in the chamber has been determined by well-defined solid angle  $\alpha$ -particle counting and amounts to an average  $\alpha$ -activity of about 1.16 MBq or an average

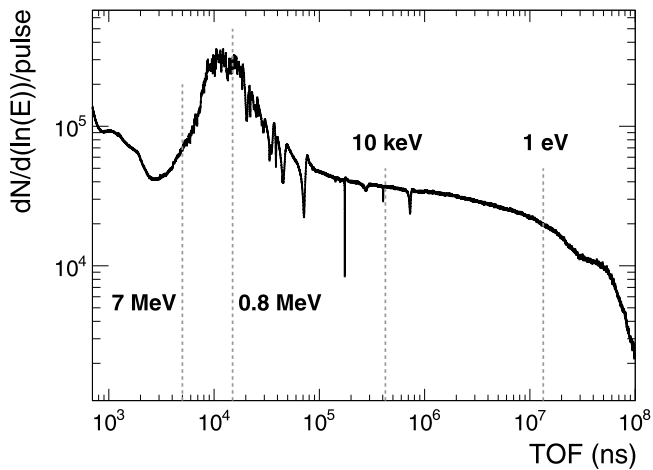


Fig. 7. Neutron fluence at n\_TOF EAR1 185 m from the source.

areal density of  $264.5 \mu\text{g}/\text{cm}^2$  per sample (with a standard deviation of  $30.9 \mu\text{g}/\text{cm}^2$  among the 14 samples), which permits fission fragments to escape the deposits, resulting in a total mass of  $46.5(3) \text{ mg}$  of  $^{233}\text{U}$ .

### 3. Fission-tagging experiment at n\_TOF

$^{233}\text{U}$  is a prime example for the application of fission tagging as it exhibits a fission cross-section which is on average a factor 10 larger than the corresponding capture cross-section. Thus, the fission reaction will introduce a background into the measurement that comprises of two components: the prompt component caused by the de-excitation of the highly excited fission products and the delayed component caused by either fission neutrons being captured in the experimental set-up or decays of unstable fission fragments with half-lives larger than a few nanoseconds up to microseconds. The prompt component causes a much larger background and appears quasi-instantaneous with the fission reaction and can be easily quantified and removed using fission-tagging. The delayed component can also be studied with fission-tagging but depends on the experimental set-up's sensitivity to neutrons and shall not be the focus of this work.

#### 3.1. Experimental set-up

##### 3.1.1. The n\_TOF facility at CERN

The n\_TOF experimental area 1 (EAR1) facility [7] is devoted for the measurement of energy dependent neutron cross-sections in an

energy range from thermal up to GeV. Neutrons are produced by a high-intensity  $20 \text{ GeV}/c$  proton beam impinging on a lead target and moderated in a borated water-layer down to thermal energies. The proton beam is delivered by CERN's Proton Synchrotron with an average proton beam intensity of  $7 \cdot 10^{12}$  or  $4 \cdot 10^{12}$  protons per bunch for dedicated or parasitic bunches respectively. The neutron fluence as a function of the arrival time in EAR1 located approximately 185 m from the lead target is shown in Fig. 7.

The n\_TOF facility provides a fully digital Data Acquisition system (DAQ) [10] and a large storage space, namely the *CERN Advanced STORAGE manager* (CASTOR) [11]. The waveforms of all signals are digitized with high performance digitizers, ADQ412 or ADQ414 [12], with 12 or 14 bit resolution respectively which are operated at 500 MSamples/s. This allows an offline analysis to be performed with dedicated pulse shape analysis routines [9]. The digitizers are triggered with a common external clock to avoid time drifts between the different channels.

##### 3.1.2. The n\_TOF Total Absorption Calorimeter

The n\_TOF Total Absorption Calorimeter TAC [6] is designed to detect in coincidence the  $\gamma$ -rays of the electro-magnetic cascade following a neutron capture event. The TAC is a segmented  $4\pi$  scintillator array consisting of 40  $\text{BaF}_2$  crystals mounted in a honeycomb structure which holds the full spherical detector shell as shown in Fig. 8. The spherical  $\text{BaF}_2$  shell has a 20 cm and 50 cm inner and outer diameter respectively, covering 95% solid angle resulting in an efficiency of detecting at least one  $\gamma$ -ray from a cascade close to 100%. To reduce the neutron sensitivity, namely the probability of detecting neutrons of the beam scattered from the in-beam materials, a so-called *absorber* is placed between the crystals and the sample to be measured. The absorber is made out of polyethylene loaded with 7.56 w% natural lithium to absorb scattered neutrons and consists of two spherical shell halves in which the fission chamber was embedded as shown in the right panel of Fig. 3. TAC events are characterized by three parameters: the time-of-flight, the number of hit crystals referred to as crystal multiplicity  $m_{cr}$  and the sum of the deposited energy in all 40 crystals  $E_{Sum}$  within a time coincidence window of  $T_{coinc}^{TAC} = 12 \text{ ns}$ .

#### 3.2. FICH Performance

##### 3.2.1. Pulse height spectrum and alpha-fission discrimination

Fig. 9 shows the pulse height spectrum of the fission chamber for neutrons of less than 10 keV energy and without neutron beam (beam off). Small pulse heights are dominated by the  $\alpha$ -particle background and are several orders of magnitude larger than the contribution of the

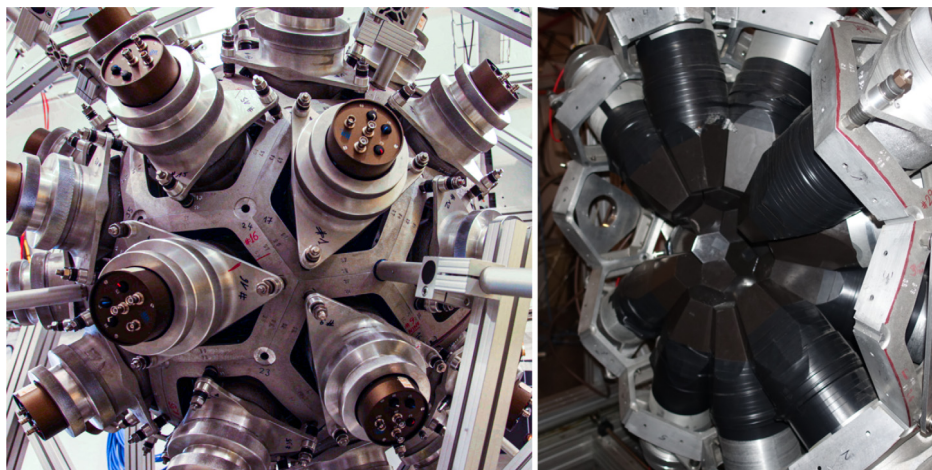


Fig. 8. Picture of the fully assembled (left) and open (right) TAC.

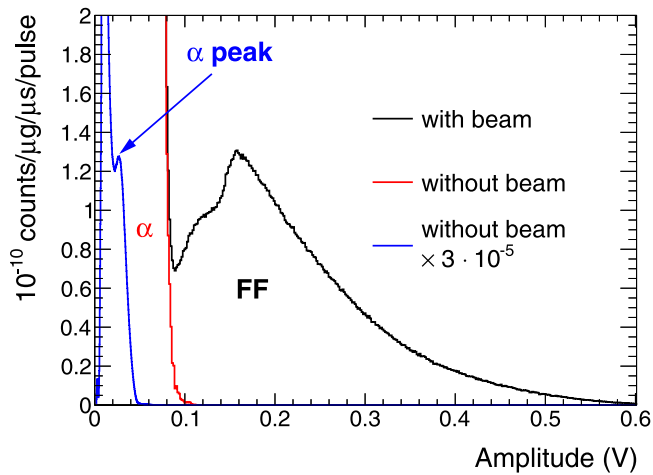


Fig. 9. Pulse height spectra of  $^{233}\text{U}$  with and without neutron beam for events with  $E_n < 10\text{ keV}$  from a single FICH channel.

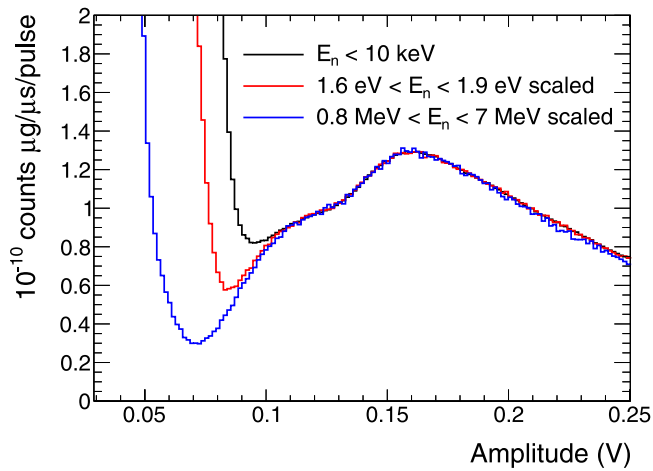


Fig. 10. Pulse height spectra for different  $E_n$  regions corresponding to different fission fragment to  $\alpha$ -particle ratios from all FICH channels.

fission events. The blue line in Fig. 9 is a scaled version (for visualization purposes) of the pulse height spectrum of the fission chamber without neutron beam and shows the  $\alpha$ -peak which corresponds to  $\alpha$ -particles that deposit their full energy in the gas.

The relatively poor separation of fission fragments and  $\alpha$ -particle background at around 0.09 V is not surprising considering the high  $\alpha$ -particle count rate. Choosing appropriate conditions allows to study the response of the FICH to fission fragments with a much better separation as shown in Fig. 10 where the pulse-height spectra for different alpha to fission ratios are displayed. For example, gating on the first and largest resonance at  $1.6\text{ eV} < E_n < 1.9\text{ eV}$ , corresponding to the TOF region of 10.6-9.7 ms, improves the separation of  $\alpha$ -particles and fission fragments. Furthermore, the characteristics of the neutron fluence at nTOF EAR1 can also be exploited by choosing the neutron energy region around of corresponding to a TOF range of 5-15  $\mu\text{s}$  (0.8-7 MeV), see Fig. 7. Due to the higher fluence in this TOF region the alpha-fission separation is further improved.

### 3.2.2. Gain monitoring

The gain of the FICH has been monitored throughout the measurement by counting the number of fission fragment (FF) events ( $> 0.1\text{ V}$ ) per nominal ( $7 \cdot 10^{12}$  protons) pulse. Fig. 11 shows the gain fluctuation of one of the ionization cells over time, indicated in RunNumber. No

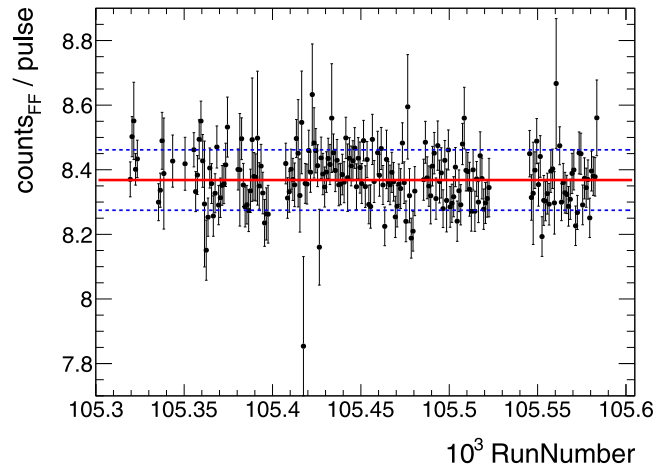


Fig. 11. Variation of the gain over time: number of events with  $\text{amp} > 0.1\text{ V}$  and  $E_n < 0.8\text{ MeV}$  per protons per run — typically 4 h per run. The red line corresponds to the weighted average of 8.36 FF counts per pulse with an uncertainty of the fit of 0.1%. The blue dashed lines indicate the standard deviation of the data points which is 1%.

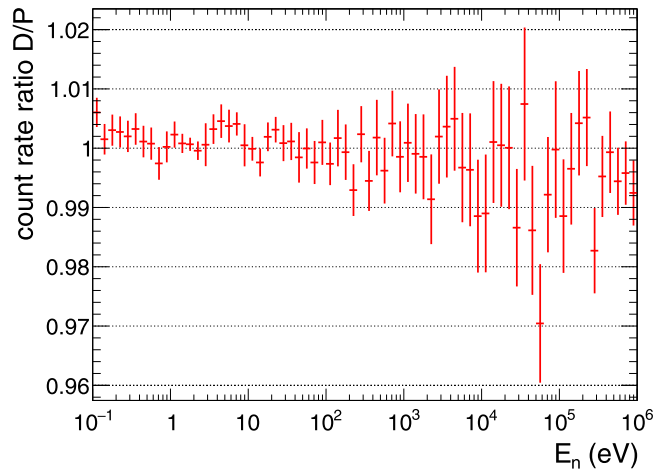


Fig. 12. Ratio of the fission count rates for dedicated (D) and parasitic (P) beam pulse types.

drift of the gain can be observed, proving a good detector stability throughout the whole measurement time of about four weeks.

### 3.2.3. Dead time and validation

With high count rates dead time and pile-up can become severe. Due to its design as a fast fission chamber, count rates of several MBq should be sustainable without the need to correct for pile-up effects in fission fragment detection. Fig. 12 shows the ratio of the count rates for dedicated (D) and parasitic (P) beam pulse types of fission events ( $\text{amp} > 0.1\text{ V}$ ). A good agreement with 1% is reached up to 1 MeV, indicating that there are no pile-up or dead time issues. The outlier around 55 keV most likely corresponds to dips in the neutron flux due to aluminium resonances, hence very low statistics.

To verify the satisfactory behaviour of the fission detector the shape of the  $^{233}\text{U}(n,f)$  cross-section has been calculated from the FICH events and the shape of the neutron flux. The resulting shape of the  $^{233}\text{U}(n,f)$  cross-section has then been normalized to evaluated libraries in the neutron energy range from 8.1 eV to 17.6 eV because this region is well separated avoiding interference from neighbouring resonances, as has been suggested in [13]. Fig. 13 shows the ratio of the scaled  $^{233}\text{U}(n,f)$

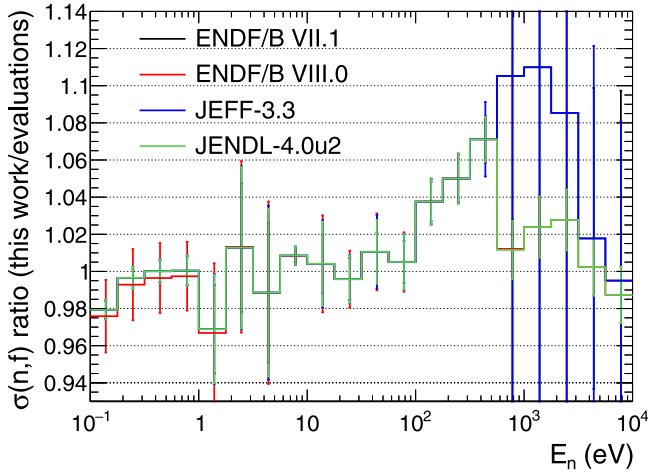


Fig. 13. Ratio between the experimentally determined cross-section, scaled to the evaluated libraries in the neutron energy range from 8.1 eV to 17.6 eV, and the corresponding evaluated library.

cross-section obtained from this work and the evaluated libraries, ENDF/B-VII.1 [14], ENDF/B-VIII.0 [15], JEFF-3.3 [16] and JENDL-4.0u2 [17], from 0.1 eV up to 10 keV. The deviations are within the evaluations' uncertainties in the resolved resonance region ( $<600$  eV) while the evaluations are discrepant in the unresolved region ( $>600$  eV). Thus, taking only the resolved resonance region into account it can be concluded that the fission chamber is working satisfactorily in the neutron energy range of this measurement ( $<10$  keV). An accurate prompt fission background subtraction for the measurement of the  $^{233}\text{U}(n, \gamma)$  can thus be assured.

### 3.3. Fission tagging

Events that produce signals in both detectors (FICH & TAC) in coincidence are related to fission events. The time correlation is given by the time difference between the detection of the event in the two detectors. Prompt fission events (small time difference) are characterized by high  $\gamma$ -multiplicity [18], as was observed and suggested in previous works [2,3].

#### 3.3.1. Event reconstruction

The coincidence algorithm is based on the use of a coincidence window  $T_{coinc}^{TAC-FICH}$  between TAC and FICH and allows positive and negative time differences. Fig. 14 shows the distribution of time differences  $\delta T = TOF_{TAC} - TOF_{FICH}$  for all found coincidences and can be explained as follows:

- Events with  $\delta T < -200$  ns show a flat distribution and correspond to random coincidences.
- The shape for  $-200$  ns  $< \delta T < -20$  ns can be described by an exponential sitting on top of the constant background. The exponential increase corresponds to events where a  $\gamma$ -ray is emitted before the nucleus fissions. These events can be explained by the existence of the  $(n, \gamma f)$  process (fission isomers) [19–22].
- A main peak for  $-10$  ns  $< \delta T < 10$  ns corresponding to the prompt fission events as suggested by the characteristics of those events with high  $E_{sum}$  and  $m_{cr}$ , indicated by the blue line.
- Another sharp structure or side peak for  $10$  ns  $< \delta T < 20$  ns is an artefact of the event reconstruction process. The time difference between the main peak and this side peak corresponds exactly to the TAC coincidence window of 12 ns which is the minimum time difference between two TAC events due to how the TAC coincidence reconstruction algorithm works. The position of the side peak will shift with the TAC coincidence window.

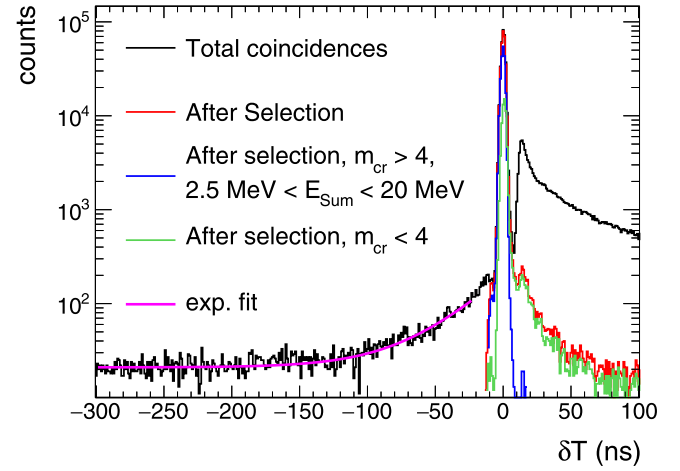


Fig. 14. Time difference distribution between TAC and FICH events. The selection refers to the algorithm that selects the corresponding prompt event, as described in the text. The features of the distribution are explained in the text.

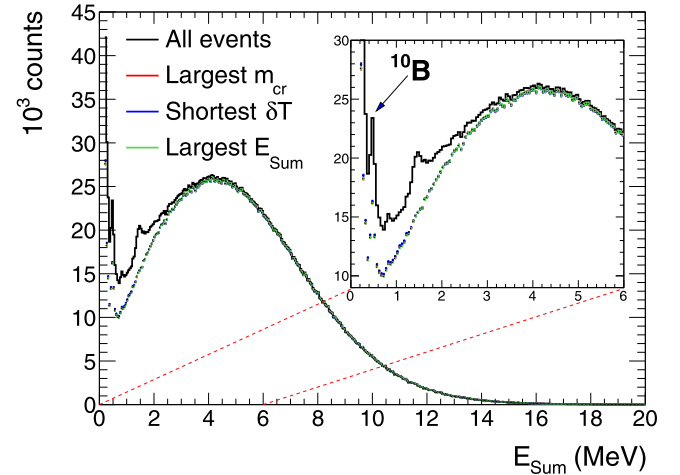


Fig. 15. Comparison of the different event selection algorithms using either largest  $E_{sum}$ , largest  $m_{cr}$  or smallest  $\delta T$  as primary criteria. In the zoom in the region for  $E_{sum} < 6$  MeV the suppression of the 480 keV  $\gamma$ -ray emitted in the  $^{10}\text{B}(n, \alpha)$  reaction and the 1435 keV  $\gamma$ -ray from inelastic scattering of fission neutrons on  $^{138}\text{Ba}$  can be observed.

- Events with  $\delta T > 20$  ns form an exponential tail and correspond to delayed events. Such events can be induced by fission neutrons which are subsequently captured in the experimental set-up thus emitting  $\gamma$ -ray cascades or isomeric states of the fission products that de-excite via  $\gamma$ -ray cascades with a delay corresponding to the half-life of the isomeric state. These events are related to fission but are not prompt fission  $\gamma$ -rays.

For reasons of causality the TAC-FICH coincidence window may not be smaller than the TAC coincidence window, otherwise there is the possibility of losing coincidences artificially. The optimal time window is a compromise between pile-up and efficient tagging.  $T_{coinc}^{TAC-FICH} > T_{coinc}^{TAC}$  can lead to multiple coincidences found for a single FICH event. The different coincidences will be characterized by different TAC events, hence different  $E_{sum}$ ,  $m_{cr}$  and  $\delta T$ . If two or more TAC events are assigned to the same FICH event, the TAC event with the highest crystal multiplicity  $m_{cr}$  is selected as the corresponding prompt fission event. If the TAC events happen to have the same crystal multiplicity then the event with higher  $E_{sum}$  is selected as the corresponding prompt fission event. In principle these criteria are arbitrary and the performance of the different event selection algorithms is illustrated in Fig. 15. It shows

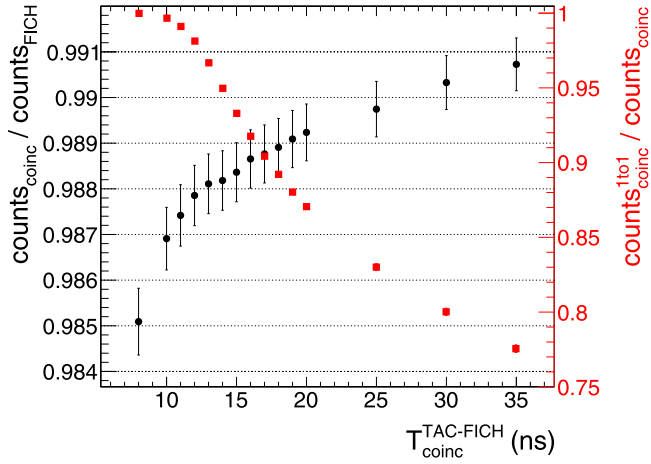


Fig. 16. Fraction of found coincidences with respect to the total number of fission events in the FICH (black dots; left axis). Fraction of events where exactly one TAC event is found for one FICH event with respect to all found coincidences (red squares; right axis). Both for events with  $amp > 0.09$  V and  $1.6 \text{ eV} < E_n < 1.9 \text{ eV}$ . Notice the different scales on the two y-axes.

the  $E_{sum}$  spectra of the corresponding prompt fission events selected with different algorithms. It is evident that no matter which algorithm is chosen the difference is negligible.

Fig. 16 shows the effect of different coincidence windows  $T^{TAC-FICH}_{coinc}$  on the total number of found coincidences normalized to the total number of fission events detected by the FICH (black dots; left axis). A steady increase can be seen with increasing  $T^{TAC-FICH}_{coinc}$  which is understandable, although those additionally found TAC events in coincidence are not necessarily related to the prompt fission event but might correspond to random or delayed events. On the other hand Fig. 16 shows the number of coincidences where exactly one TAC event is found for one FICH event (red squares; right axis). With increasing coincidence window  $T^{TAC-FICH}_{coinc}$  the number of one to one coincidences drastically decreases, as the probability of multiple tagging starts to increase. A coincidence window  $T^{TAC-FICH}_{coinc}$  slightly larger than the  $T^{TAC}_{coinc}$  is already sufficient to tag close to 99% of the FICH events while a window too large might result in an uncertain assignment of multiple TAC events to a FICH event. To reduce this uncertainty the  $T^{TAC-FICH}_{coinc}$  coincidence window is set to 14 ns.

FICH-TAC coincidence tagging also allows for a better alpha-fission separation as the probability of tagging an  $\alpha$ -particle is negligible compared to a fission fragment. In Fig. 17 the tagged fission amplitude spectra for different  $E_n$  regions are compared to the amplitude spectra of the best achievable separation solely using the FICH. The improvement is obvious and allows the investigation of the shape of the fission fragment energy deposition in the fission chamber below what was possible with the FICH alone. It shall be noted that the TAC data for  $0.8 \text{ MeV} < E_n < 7 \text{ MeV}$  is usually not used in the analysis of cross-sections due to the so-called  $\gamma$ -flasheffect [6,7,23] which blinds the detector.

### 3.3.2. Tagging and FICH efficiency

In analogy to previous works [2,4], the tagging efficiency  $\epsilon_{Tagg}(A_{th}; E_{sum}, m_{cr})$  describes the probability of detecting a fission event identified as such by the FICH in the TAC and depends on the applied amplitude threshold  $A_{th}$ . It is defined as the ratio between the tagged fission events  $c_{Tagg}(A_{th}; E_{sum}, m_{cr})$  and the total fission counts detected by the TAC  $c_{Fiss-TAC}(E_{sum}, m_{cr})$  (dependencies on  $E_{sum}$  and  $m_{cr}$  are implicit for readability):

$$\epsilon_{Tagg}(A_{th}) = \frac{c_{Tagg}(A_{th})}{c_{Fiss-TAC}} \quad (1)$$

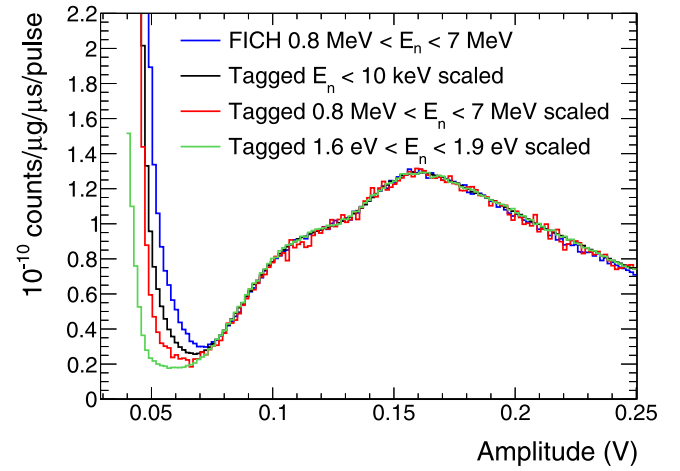


Fig. 17. Pulse height spectra of the events in the fission chamber for  $0.8 \text{ MeV} < E_n < 7 \text{ MeV}$  compared to tagged events for different  $E_n$  regions from all FICH channels. The neutron flux of  $n_{TOF}$  can be seen in Fig. 7.

The fission detection efficiency  $\epsilon_{FICH}(A_{th})$  is the probability of detecting a fission reaction by the FICH detector and depends only on the amplitude threshold  $A_{th}$  applied to the FICH events.

Under the assumption that the probability of detecting a fission event in one of the detectors does not depend on whether it was detected in the other one, the tagging efficiency  $\epsilon_{Tagg}$  and the fission detection efficiency  $\epsilon_{FICH}$  are the same quantity and the tagging efficiency depends only on the applied amplitude threshold  $A_{th}$ .

Following equation (1)  $c_{Tagg}$  and  $c_{Fiss-TAC}$  have to be determined to calculate the tagging efficiency. While the tagged counts  $c_{Tagg}$  can be taken directly from the coincidence algorithm, the TAC events corresponding to fission reactions  $c_{Fiss-TAC}$  have to be cleaned from the background first. The background consists of the ambient, the neutron beam induced and the sample induced background. The  $^{233}\text{U}(n, \gamma)$  reaction sets the lower threshold for the sum energy as the calculation will be biased if sum energies below the neutron separation energy of  $^{234}\text{U}$   $S_n(^{233}\text{U} + n) = 6.85 \text{ MeV}$  are considered. Thus as a general rule the efficiency will only be calculated for  $E_{sum} > 8 \text{ MeV}$  to avoid this component of the background completely. Dedicated measurements of the ambient and neutron beam induced background have been performed to estimate their contribution to the overall background. Furthermore, the background subtraction is less prone to uncertainties and statistical fluctuations for high crystal multiplicity and large sum energies because there is little background for such conditions but a compromise between systematic and statistical uncertainties has to be made. Nevertheless, the sensitivity with respect to the applied conditions in crystal multiplicity and sum energy has to be investigated and is shown for two different amplitude thresholds  $A_{th}$  in Fig. 18. Even though the residual background is subtracted a variation for lower multiplicities can be observed that decreases with increasing multiplicities. For  $m_{cr} > 6$  the variation of the calculated efficiency becomes smaller than the statistical uncertainty, indicating that only fission events are left in the calculation. One potential explanation for the systematic trend could be additional background components i.e. reactions induced by scattered (from the samples) or fission neutrons. Indeed, neutrons emitted in the fission process can be captured, preferably in the  $\text{BaF}_2$  crystals themselves leading to TAC events with large deposited energies. This might also explain why the calculated efficiency in Fig. 18 shows a stronger dependence on the multiplicity for  $E_{sum} > 8 \text{ MeV}$  compared to the more restrictive condition  $E_{sum} > 10 \text{ MeV}$ , as the fission neutron induced background should not exceed  $10 \text{ MeV}$  sum energy according to the neutron separation energies of barium isotopes, i.e.  $S_n(^{135}\text{Ba} + n) = 9.1 \text{ MeV}$ .

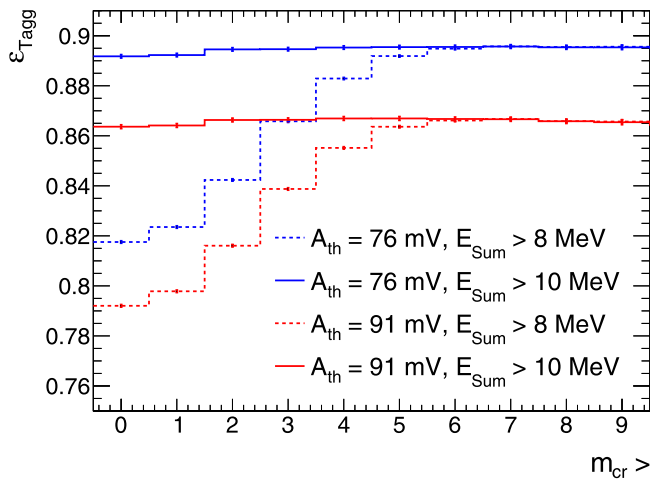


Fig. 18. Fission tagging efficiency  $\varepsilon_{Tagg}$  as a function of the crystal multiplicity and sum energy for two different amplitude thresholds  $A_{th}$  in the neutron energy interval from 1.6 eV to 1.9 eV.

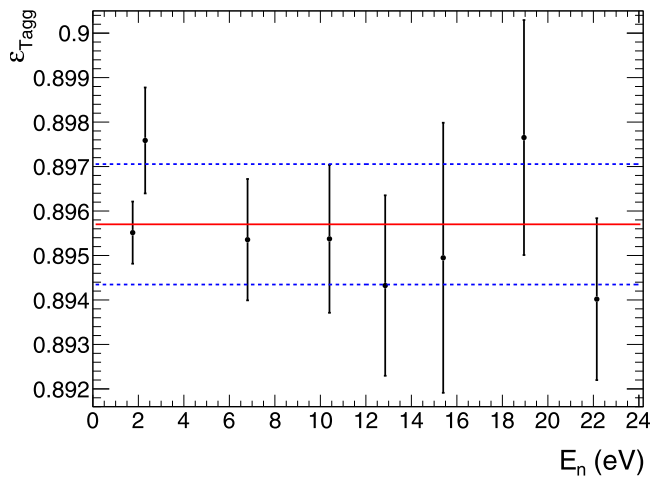


Fig. 19. Fission tagging efficiency calculated in several neutron resonances for  $A_{th} = 0.076$  V,  $m_{cr} > 6$  and  $E_{Sum} > 10$  MeV, their weighted average (red line) and the standard deviation of the data points (blue dashed lines). The uncertainties are calculated from the two highly correlated quantities in Eq. (1).

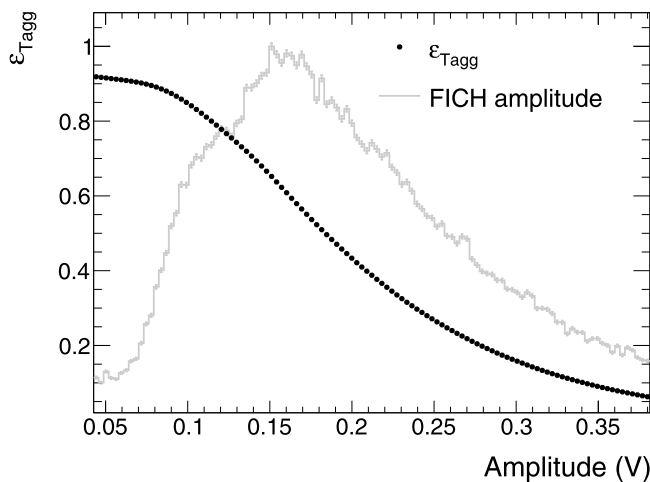


Fig. 20. Tagging efficiency  $\varepsilon_{Tagg}$  as a function of the FICH amplitude threshold (black circles). A scaled FICH amplitude spectrum in coincidence with the TAC for events with  $m_{cr} > 6$  and  $E_{Sum} > 10$  MeV is shown too (grey line) as it is directly related to the efficiency.

Fig. 18 shows that for  $m_{cr} > 6$  the sensitivity to the background is reduced within error bars as both conditions in  $E_{Sum}$  coincide.

Using only events with  $m_{cr} > 6$  and  $E_{Sum} > 10$  MeV the efficiency was calculated in several neutron resonances in order to verify a possible variation. The values of the efficiency for the used amplitude threshold  $A_{th} = 0.076$  V were all in agreement within their uncertainties, as shown in Fig. 19. Thus the average tagging efficiency over all neutron energy intervals is calculated to  $\varepsilon_{Tagg}(A_{th} = 0.076$  V) = 89.6(1) % and shown as a function of the fission amplitude threshold in Fig. 20. The latter allows to calculate the tagging efficiency for any given amplitude cut and shows the stability of the value of  $\varepsilon_{Tagg}(A_{th} = 0.076$  V) with respect to small gain fluctuations, which are equivalent to small variations in the amplitude threshold. This gives further confidence in the accuracy of the tagging efficiency, which is crucial to assess the capture cross section.

In the measurement of the  $^{233}\text{U}$   $\alpha$ -ratio the capture response is obtained by subtracting the efficiency corrected tagged counts from the total counts in the calorimeter. Without giving a detailed calculation, from the  $^{233}\text{U}$  capture and fission cross-sections it can be expected that an uncertainty in the tagging efficiency of 0.1 % translates into a 1 % uncertainty in the  $^{233}\text{U}$   $\alpha$ -ratio on average. The results show that this detector is well suited to obtain an accurate alpha-ratio.

#### 4. Conclusions

A new compact fission chamber was developed and optimized for the use in fission tagging experiments to measure capture cross-sections of fissile isotopes. The development aimed at the use of the detection system at the n\_TOF facility (CERN), coupled to the Total Absorption Calorimeter of EAR1, but can be generalized to other set-ups. The fission chamber was optimized for timing performance with an average signal rise time of about 16 ns and a FWHM of 34 ns which is optimal for the high specific  $\alpha$ -particle count rates from  $^{233}\text{U}$  as well as the alpha-fission discrimination and allows using a narrow coincidence window between the calorimeter and the FICH facilitating low pile-up in the coincidence reconstruction. Its compactness hosting a total of 14 samples as well as the minimal amount of structural material in beam provide excellent conditions for low background and high statistics measurements. The whole experimental set-up was further designed to achieve good performance, especially stability over time as well as effectively tagging the fission events with an efficiency close to 90 %.

An experiment aiming at measuring the  $^{233}\text{U}(n, \gamma)$  cross-section was performed and the results have shown that the developed fission chamber is well suited to tag the prompt fission  $\gamma$ -rays, hence to have a good control over the fission background in the capture measurement. Results of this measurement will be presented in a separate publication.

#### Declaration of competing interest

The authors declare that they have no known competing financial interests or personal relationships that could have appeared to influence the work reported in this paper.

#### CRediT authorship contribution statement

**M. Bacak:** Software, Validation, Visualization, Investigation, Formal analysis, Writing - original draft, Data curation. **M. Aïche:** Methodology. **G. Bélier:** Conceptualization, Investigation, Methodology, Resources, Writing - review & editing. **E. Berthoumieux:** Software, Validation, Investigation, Conceptualization, Methodology, Project administration, Writing - review & editing, Data curation, Supervision. **M. Diakaki:** Investigation, Conceptualization, Methodology, Writing - review & editing. **E. Dupont:** Investigation, Conceptualization, Methodology, Project administration, Writing - review & editing, Funding acquisition, Data curation, Supervision. **F. Gunsing:** Investigation, Conceptualization, Methodology, Project administration, Writing - review & editing,

Funding acquisition, Data curation, Supervision. **J. Heyse:** Investigation, Methodology, Project administration. **S. Kopecky:** Investigation, Resources. **B. Laurent:** Conceptualization, Investigation, Methodology, Resources, Writing - review & editing. **H. Leeb:** Resources. **L. Mathieu:** Investigation, Methodology, Writing - review & editing. **A. Moens:** Resources. **S. Richter:** Resources. **P. Schillebeeckx:** Investigation. **O. Serot:** Investigation. **G. Sibbens:** Resources. **J. Taieb:** Conceptualization, Investigation, Methodology, Resources, Writing - review & editing. **D. Vanleeuw:** Resources. **V. Vlachoudis:** Software.

## Acknowledgements

This work was partially supported by the French NEEDS/NACRE Project and by the European Commission within HORIZON2020 via the EURATOM Project EUFRAT.

## References

- [1] L.W. Weston, et al., *Nuc. Sci. Eng.* 34 (1968) 1, <http://dx.doi.org/10.13182/NSE68-A19361>.
- [2] C. Guerrero, et al., *Eur. Phys. J. A* 48 (2012) 29, <http://dx.doi.org/10.1140/epja/i2012-12029-2>.
- [3] M. Jandel, et al., *Phys. Rev. Lett.* 109 (2012) 202506, <http://dx.doi.org/10.1103/PhysRevLett.109.202506>.
- [4] J. Balibrea-Correa, et al., *EPJ Web Conf.* 146 (2017) 11021, <http://dx.doi.org/10.1051/epjconf/201714611021>.
- [5] I. Companis, et al., *EPJ Web Conf.* 69 (2014) 00005, <http://dx.doi.org/10.1051/epjconf/20136900005>.
- [6] C. Guerrero, et al., *Nucl. Instrum. Methods A* 608 (2009) 424–433, <http://dx.doi.org/10.1016/j.nima.2009.07.025>.
- [7] C. Guerrero, A. Tsinganis, E. Berthoumieux, et al., *Eur. Phys. J. A* 49 (2013) 27, <http://dx.doi.org/10.1140/epja/i2013-13027-6>.
- [8] J. Taieb, B. Laurent, G. Bélier, A. Sardet, C. Varignon, *Nucl. Instrum. Methods A* 833 (2016) 1, <http://dx.doi.org/10.1016/j.nima.2016.06.137>.
- [9] P. Žugec, et al., *Nucl. Instrum. Methods A* 812 (2016) 134, <http://dx.doi.org/10.1016/j.nima.2015.12.054>.
- [10] A. Masi, et al., *International Conference on Accelerator and Large Experimental Control Systems*, vol. 49, 2018, pp. 1900–1905, <http://dx.doi.org/10.18429/JACoW-ICALEPCS2017-THPHA195>.
- [11] CERN, CERN Advanced storage manager, 2019, URL [castor.web.cern.ch](http://castor.web.cern.ch).
- [12] SP Devices, The SP devices website, 2019, URL <https://www.spdevices.com/>.
- [13] A.J. Deruytter, C. Wagemans, *Nucl. Sci. Eng.* 54 (1974) 423–431, <http://dx.doi.org/10.13182/NSE74-A23436>.
- [14] M.B. Chadwick, et al., *Nucl. Data Sheets* 112 (2011) 2887–2996, <http://dx.doi.org/10.1016/j.nds.2011.11.002>.
- [15] D.A. Brown, et al., *Nucl. Data Sheets* 148 (2018) 1–142, <http://dx.doi.org/10.1016/j.nds.2018.02.001>.
- [16] JEFF team, 2017, URL <https://www.oecd-nea.org/dbdata/jeff/jeff33/>.
- [17] K. Shibata, et al., *J. Nucl. Sci. Technol.* 48 (2011) 1–30, <http://dx.doi.org/10.1080/18811248.2011.9711675>.
- [18] K.H. Schmidt, et al., *Nucl. Data Sheets* 131 (2016) 107–221, <http://dx.doi.org/10.1016/j.nds.2015.12.009>.
- [19] V. Stavinsky, M.O. Shaker, *Nucl. Phys.* 62 (1965) 667–672, [http://dx.doi.org/10.1016/0029-5582\(65\)90589-4](http://dx.doi.org/10.1016/0029-5582(65)90589-4).
- [20] J.E. Lynn, *Phys. Lett.* 18 (1965) 31–34, [http://dx.doi.org/10.1016/0031-9163\(65\)90020-X](http://dx.doi.org/10.1016/0031-9163(65)90020-X).
- [21] P. Talou, et al., *EPJ Web Conf.* 112 (2016) 01013, <http://dx.doi.org/10.1051/epjconf/201612201013>.
- [22] J.E. Lynn, et al., *Phys. Rev. C* 97 (2018) 064601, <http://dx.doi.org/10.1103/PhysRevC.97.064601>.
- [23] F.K. N. Colonna, *Prog. Part. Nucl. Phys.* 101 (2018) 177–203, <http://dx.doi.org/10.1016/j.pnpnp.2018.02.002>.